



WiMeasure: Millimeter-level Object Size Measurement with Commodity WiFi Devices

XUANZHI WANG, Peking University, China

KAI NIU, Peking University, China and Beijing Xiaomi Mobile Software Company Ltd., China

ANLAN YU, Peking University, China

JIE XIONG, University of Massachusetts Amherst, United States

ZHIYUN YAO, JUNZHE WANG, and WENWEI LI, Peking University, China

DAQING ZHANG*, Peking University, China and Institut Polytechnique de Paris, France

In the past few years, a large range of wireless signals such as WiFi, RFID, UWB and Millimeter Wave were utilized for sensing purposes. Among these wireless sensing modalities, WiFi sensing attracts a lot of attention owing to the pervasiveness of WiFi infrastructure in our surrounding environments. While WiFi sensing has achieved a great success in capturing the target's motion information ranging from coarse-grained activities and gestures to fine-grained vital signs, it still has difficulties in precisely obtaining the target size owing to the low frequency and small bandwidth of WiFi signals. Even Millimeter Wave radar can only achieve a very coarse-grained size measurement. High precision object size sensing requires using RF signals in the extremely high-frequency band (e.g., Terahertz band). In this paper, we utilize low-frequency WiFi signals to achieve accurate object size measurement without requiring any learning or training. The key insight is that when an object moves between a pair of WiFi transceivers, the WiFi CSI variations contain singular points (i.e., singularities) and we observe an exciting opportunity of employing the number of singularities to measure the object size. In this work, we model the relationship between the object size and the number of singularities when an object moves near the LoS path, which lays the theoretical foundation for the proposed system to work. By addressing multiple challenges, for the first time, we make WiFi-based object size measurement work on commodity WiFi cards and achieve a surprisingly low median error of 2.6 mm. We believe this work is an important missing piece of WiFi sensing and opens the door to size measurement using low-cost low-frequency RF signals.

CCS Concepts: • **Human-centered computing** → **Ubiquitous and mobile computing systems and tools**; *Ubiquitous computing*; *Mobile computing*; Ambient intelligence.

Additional Key Words and Phrases: WiFi sensing, size measurement, diffraction effect, wireless sensing

ACM Reference Format:

Xuanzhi Wang, Kai Niu, Anlan Yu, Jie Xiong, Zhiyun Yao, Junzhe Wang, Wenwei Li, and Daqing Zhang. 2023. WiMeasure: Millimeter-level Object Size Measurement with Commodity WiFi Devices. *Proc. ACM Interact. Mob. Wearable Ubiquitous Technol.* 7, 2, Article 79 (June 2023), 26 pages. <https://doi.org/10.1145/3596250>

*Corresponding author.

Authors' addresses: [Xuanzhi Wang](#), Key Laboratory of High Confidence Software Technologies (Ministry of Education), school of Computer Science, Peking University, Beijing, China, xuanzhiwang@stu.pku.edu.cn; [Kai Niu](#), Peking University, Beijing, China and Beijing Xiaomi Mobile Software Company Ltd., Beijing, China; [Anlan Yu](#), Peking University, Beijing, China; [Jie Xiong](#), University of Massachusetts Amherst, Amherst, United States; [Zhiyun Yao](#); [Junzhe Wang](#); [Wenwei Li](#), Peking University, Beijing, China; [Daqing Zhang](#), School of Computer Science, Peking University, Beijing, China, Telecom SudParis and Institut Polytechnique de Paris, Evry, France, dqzhang@sei.pku.edu.cn.

Permission to make digital or hard copies of all or part of this work for personal or classroom use is granted without fee provided that copies are not made or distributed for profit or commercial advantage and that copies bear this notice and the full citation on the first page. Copyrights for components of this work owned by others than ACM must be honored. Abstracting with credit is permitted. To copy otherwise, or republish, to post on servers or to redistribute to lists, requires prior specific permission and/or a fee. Request permissions from permissions@acm.org.

© 2023 Association for Computing Machinery.

2474-9567/2023/6-ART79 \$15.00

<https://doi.org/10.1145/3596250>

1 INTRODUCTION

WiFi technologies have achieved a huge success in connecting end-user devices such as smartphones and laptops to the Internet. Beyond conventional wireless data communication, recent research has sought to sense targets in a contact-free manner leveraging pervasive WiFi signals. The basic principle is that target's movements can induce variations at the received WiFi signals. By modeling and quantifying the relationship between target's movements and the corresponding signal variations, target context such as movement speed and displacement can be obtained. WiFi sensing has enabled a large variety of applications including passive localization and tracking [25, 26, 37, 38, 49, 50, 52], gesture/activity recognition [4, 15, 20, 34, 48, 58, 59, 62] and vital sign monitoring [30, 35, 43, 46, 55, 60].

While WiFi sensing has achieved promising performance on motion sensing, it still has difficulties being used for size measurements. The fundamental principle behind size measurement is to capture the point clouds of the target by projecting narrow-beam signals at the target and obtaining accurate time information of the reflection points. To form a narrow beam, high frequency and large antenna array are required. To obtain accurate time information, large bandwidth is required. Therefore, to capture fine-grained size information, LiDAR is usually the choice and has been widely adopted in automobiles. For RF signals, the latest commodity mmWave Radar using signals in the frequency range of 76 GHz to 79 GHz achieves a much lower imaging resolution. Highly accurate imaging and size measurement can only be achieved using terahertz signals in the frequency range of 300 GHz to 3000 GHz.

Therefore, it is fundamentally challenging to use low-frequency signals such as WiFi to obtain size information of a target. On the other hand, size measurement plays an important role in logistics and industrial manufacturing. For instance, objects are classified by size in logistics to save storage space, while the product size needs to be strictly checked for quality control before products are off the assembly line. Traditionally, ruler, caliper and gauge are employed to measure object size. However, these measurement devices need to touch the objects. On the other hand, contact-free method is appealing in a lot of real-life scenarios. Camera, LiDAR and Radar are the representative devices for contact-free size measurements. Camera-based methods use optical images and distance information to extract the target's size information [51]. While highly accurate measurement can be achieved, camera-based methods require an unobstructed view of the object in good lighting conditions, which is not always available. On the other hand, RF-based methods can penetrate through the case to obtain the information of target inside. While LiDAR and Radar can capture the target shape information, obtaining accurate size information is still non-trivial due to the varying target distance. To obtain the true size information of targets, distance and signal strength information are usually required to further infer an object's size. However, even with advanced signal processing and machine learning, the accuracy of size measurement is still limited to a few centimeters [10]. As a comparison, in this work, we achieve *target size measurements at an accuracy on the scale of millimeter using cheap WiFi devices without a need of any learning or training*.

Based on our experiments, we observe a very interesting phenomenon when an object moves across the LoS (line-of-sight) path between a pair of WiFi transceivers as shown in Figure 1a. We can see that during the process of object movement, the CSI (channel state information) readings experience a sudden and drastic change (termed as *singularity*) on the I-Q plane as shown in Figure 1b. What is more interesting is that the number of singularities is related to the size, i.e., the width of the object.

To deeply understand the principle behind this phenomenon, we model the relationship between CSI variation and the target movement. As shown in Figure 1a, when the object is near the LoS path, diffraction dominates [59, 60]. Signals propagate through LoS path and also get diffracted through the boundary of the object to arrive at the receiver. When the object moves away from the LoS path, the path length difference from the upper boundary and lower boundary varies accordingly. In this paper, we theoretically prove that singularity occurs when the path length difference is exactly the integer multiple of the signal wavelength. We further show that

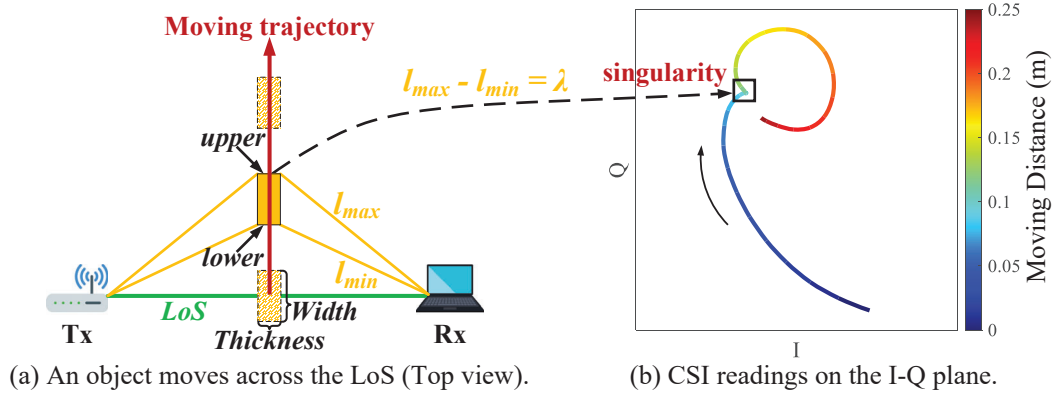


Figure 1. A singularity occurs on the CSI trajectory when a metal plate moves across the LoS path.

the number of singularities is quantitatively related to the object size (i.e., width¹ in Figure 1a), the LoS distance and object's moving trajectory. In a real-life setup, the transmitter and receiver locations are usually fixed. On a real-world production/assembly line, the object moving trajectory is also fixed. We can therefore use the number of singularities to measure the object size.

Though theoretically promising, challenges exist before we can turn this idea into a working system. The key challenge is that the singularity is an abrupt direction change of the CSI trajectory on the I-Q plane but not a power jump. It can be undetected due to the large noise of the CSI readings collected from commodity WiFi devices. Instead of using the CSI reading from one single antenna for size measurement, we employ the ratio between CSI readings collected from two antennas to mitigate the CSI noise. The derivative of the CSI ratio is further leveraged to strengthen the singularity in order to be detected. Extensive real-world experiments demonstrate that our system can robustly classify boxes of different sizes commonly used in logistics and accurately measure the object size.

The main contributions of this work are summarized as follows:

- To the best of our knowledge, this work is the first one to enable accurate object size measurement using WiFi signals.
- We model the effect of object movement on CSI signal variation and further quantify the relationship between the number of singularities on CSI variations and target size, providing the theoretical foundation of measuring an object's size using WiFi signals.
- To achieve accurate and robust size measurement using commodity WiFi devices, we adopt the CSI ratio to mitigate hardware noise and apply the CSI derivative operation to enhance the singularity for detection.
- We implement the proposed system *WiMeasure* and show that our system can classify boxes of different sizes in logistics at an accuracy close to 100% and measure the target size at a median error of 2.6 mm.

2 MODELING DIFFRACTION EFFECT FOR OBJECT SIZE MEASUREMENT

In this section, we first introduce the model to characterize the diffraction effect of a static object located near the LoS path of a WiFi transceiver pair. Then we characterize the relationship between CSI variation and object

¹In this work, we define the object side vertical to the LoS as width and the side parallel to the LoS as thickness.

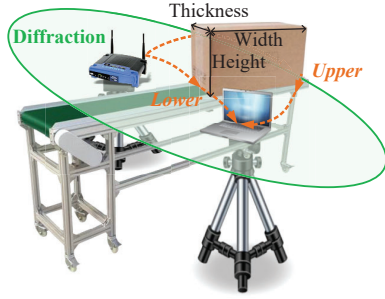


Figure 2. Working scene.

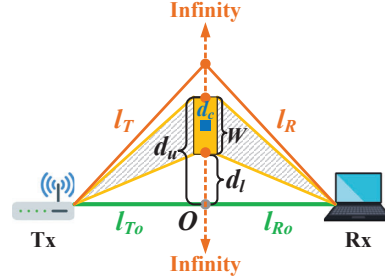


Figure 3. Diffraction model.

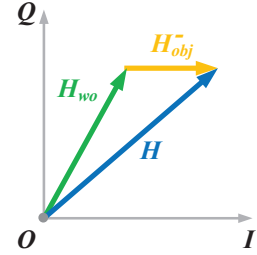


Figure 4. Signal on I-Q plane.

movement. Finally, we analyze the impact of object size and LoS distance on the number of singularities and quantify the relationship between them.

2.1 Diffraction Effect with a Static Object

As shown in Figure 2, given a pair of WiFi transceivers, the diffraction effect dominates when one object is in the nearby area of LoS (green area), while reflection becomes dominant when the object is further away from the LoS path. When there is an object located near the LoS, the signals are diffracted through the upper and lower boundaries of the object.

To characterize the effect of diffraction, we employ both amplitude and phase variations of the CSI. Specifically, when an object with a finite size is located in the diffraction area, the signals received at the receiver can be grouped into two parts: the signal through the upper area of the object and the signal through the lower area of the object as shown in Figure 3. The received signal is the sum of them and can be denoted as

$$H = H_u + H_l = \frac{i}{2\lambda} \int_{d_u}^{\infty} \frac{A}{l_T l_R} e^{-i\frac{2\pi(l_T+l_R)}{\lambda}} dx + \frac{i}{2\lambda} \int_{-\infty}^{d_l} \frac{A}{l_T l_R} e^{-i\frac{2\pi(l_T+l_R)}{\lambda}} dx, \quad (1)$$

where H_u and H_l are the CSIs for signals through the upper and lower areas of the object, respectively, λ is the signal wavelength, and A is the amplitude of the signals. H_u can be obtained by integration of the signal from the upper boundary of the object d_u to infinity, where d_u is the vertical distance from the upper boundary of the object to the LoS path. $l_T = \sqrt{l_{To}^2 + x^2}$ and $l_R = \sqrt{l_{Ro}^2 + x^2}$ are the path lengths from the integral point with a vertical height of x to the transmitter (Tx) and receiver (Rx), respectively. And l_{To} (l_{Ro}) is the distance from the vertical projection point, O on the LoS to transmitter (receiver). As a comparison, H_l is the integration of the signal from the negative infinity to the lower boundary of the object. Based on the Babinet's principle [6], we can rewrite Equation 1 as below with the object's width (W) as a variable

$$H = H_{wo} - H_{obj} = H_{wo} - \frac{i}{2\lambda} \int_{d_c - \frac{W}{2}}^{d_c + \frac{W}{2}} \frac{A}{l_T l_R} e^{-i\frac{2\pi(l_T+l_R)}{\lambda}} dx, \quad (2)$$

where H_{wo} is the signal without object (i.e., the integral from negative infinity to positive infinity), while H_{obj} is the signal shadowed by the object. d_c is the vertical distance from the center of the object to the LoS path, and W is the object width. To further analyze the signal pattern, we visualize the signal in Equation 2 as a vector on the I-Q plane. For the purpose of simplification, we employ H_{obj}^- to represent $-H_{obj}$ so that the received signal is the vector addition of H_{wo} and H_{obj}^- on the I-Q plane in Figure 4.

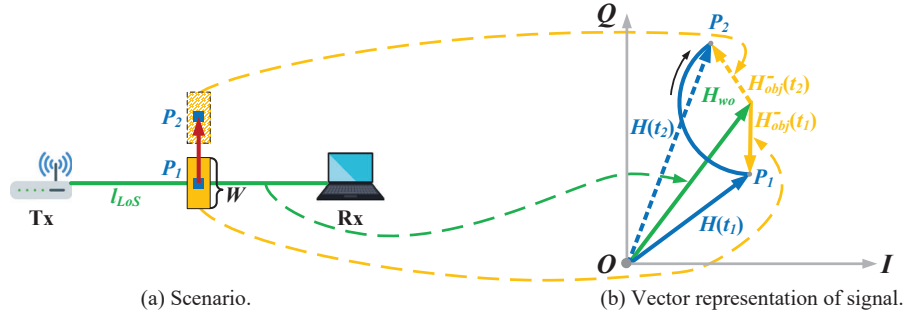
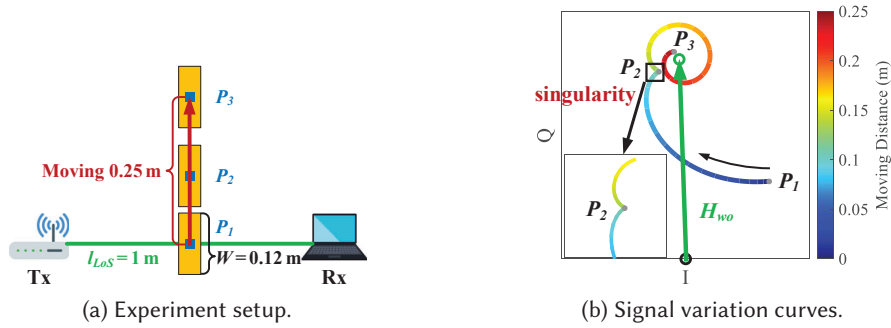


Figure 5. Diffraction effect for a moving target.


 Figure 6. The object moves upwards for a distance of 0.25 m and induces a singularity on the CSI signal curves at location P_2 .

2.2 Diffraction Effect with a Moving Object

If an object moves in the diffraction area, Equation 2 can be further expressed as

$$H(t) = H_{wo} - H_{obj}(t) = H_{wo} - \frac{i}{2\lambda} \int_{d_c(t) - \frac{W}{2}}^{d_c(t) + \frac{W}{2}} \frac{A}{l_T l_R} e^{-i \frac{2\pi \cdot L}{\lambda}} dx, \quad (3)$$

where $d_c(t)$ is the vertical distance from the center of the object to the LoS path at time t , and $L = l_T + l_R$ is the diffraction path length. Given a pair of transceivers with a fixed LoS distance, the signal without object H_{wo} can be assumed unchanged during the moving process and is a static signal, while the diffraction signal $H_{obj}(t)$ induced by object varies significantly with object's location. Especially, as the wavelength of WiFi signal is only a few centimeters (e.g., 6 cm for 5 GHz WiFi signal), centimeter-level diffraction path length change introduced by object's movement will generate significant phase change at the CSI signal (i.e., $e^{-i \frac{2\pi \cdot L}{\lambda}}$). For instance, a diffraction phase length change of 1 cm will introduce a phase variation of 60° for 5 GHz WiFi signal. On the complex plane, the phase change makes the diffraction signal vector H_{obj}^- rotates with respect to the static signal vector H_{wo} , inducing varying received signal vector $H(t)$. Specifically, the rotation pattern depends on the object's moving trajectory $d_c(t)$ and the object's width W . When the object moves away from the Tx-Rx pair, the diffraction signal vector H_{obj}^- rotates clockwise with respect to the static signal vector H_{wo} as shown in Figure 5b and vice versa. For instance, for an object with a width of 12 cm moving from 0 cm (P_1) to 25 cm (P_3) with a LoS length of 1 m as shown in Figure 6a, the theoretical signal variation pattern based on Equation 3 is shown in Figure 6b. We

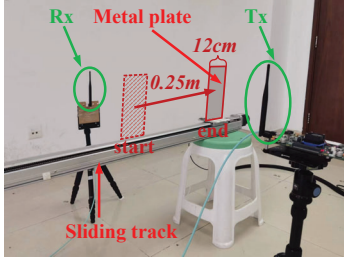


Figure 7. Experiment setup.

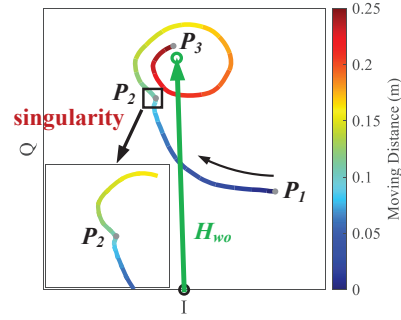


Figure 8. Benchmark experiment shows a singularity occurs on the signal curves induced by object movement.

can observe that there is a sharp and sudden change (termed as singularity) at location P_2 . We theoretically prove that the number of singularities is closely related to object's width in Section 2.3. We next design benchmark experiments to validate the proposed theory.

2.2.1 Experiment Setup. To collect CSI signals for benchmark experiments, we employ the widely used software-defined radio WARP V3 as our experiment platform. Experiments with commodity WiFi card (i.e., Intel 5300) will be presented in Section 5. The two RF interfaces of WARP are configured as the transmitter and receiver respectively and equipped with omnidirectional antennas. The two antennas are placed one meter apart with a height of 0.65 m using tripods. A sliding track with a length of 1 m is employed to move the metal plate (i.e., target) at a constant speed. As shown in Figure 7, we let the metal plate with a size of 12×25 cm move along the perpendicular bisector of the transmitter-receiver pair, starting from $d_c(start) = 0$ and stopping at $d_c(end) = 0.25$ m. The sliding track is aligned with the perpendicular bisector of the transmitter-receiver pair. The transmitter sends out WiFi packets at a rate of 1000 pkt/s on the 5.32 GHz WiFi band with a channel bandwidth of 20 MHz.

2.2.2 Experiment Results. As shown in Figure 8, we observe that the collected CSI trajectory matches the theoretical curve (Figure 6) very well. Specifically, the diffraction signal vector rotates counterclockwise with respect to the static signal vector as the plate moves away from the LoS path. One singularity exists on the collected CSI trajectory when the object moves to the position 0.12 m from the LoS path, which matches the theoretical analysis and demonstrates the correctness of the proposed model.

2.3 The Quantitative Relationship between Diffraction Signal and Size of Moving Object

To explore when and where a singularity occurs, we employ curvature to characterize the direction change rate of the points on the curve. As signal H_{wo} in Equation 3 can be assumed unchanged during the movement process, we concentrate on the diffraction signal induced by the moving object. We first present the definition of curvature for the diffraction signal vector on the I-Q plane [16] as

$$\kappa = \frac{|\varphi' \omega'' - \omega' \varphi''|}{(\varphi'^2 + \omega'^2)^{\frac{3}{2}}}, \quad (4)$$

where $\varphi = \text{real}(H_{obj}(t))$ and $\omega = \text{imag}(H_{obj}(t))$ are the real part and imaginary part of the diffraction signal vector $H_{obj}(t)$, respectively. The larger the curvature is, the more abrupt the curve direction varies. When the curvature approaches infinity (i.e., the denominator of Equation 4 is zero), a singularity occurs on the curve. Thus, a singularity on the curve should meet the following condition

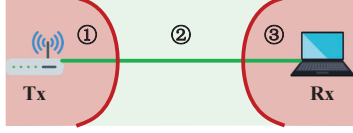


Figure 9. Regions for extracting signal singularities.

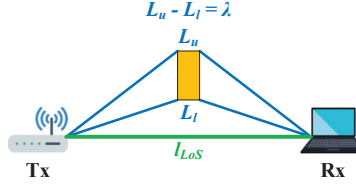


Figure 10. The relationship between the singularity of diffraction signal and the object width.

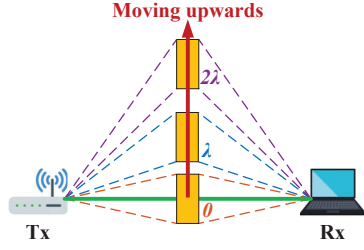


Figure 11. Location affects the path length difference and accordingly the number of singularities.

$$\varphi'^2 + \omega'^2 = 0. \quad (5)$$

Specifically, based on Equation 3, the real part of diffraction signal vector $\varphi(t)$ is $-\frac{1}{2\lambda} \int_{d_c(t)-\frac{W}{2}}^{d_c(t)+\frac{W}{2}} \frac{A}{l_T l_R} \sin \frac{2\pi L}{\lambda} dx$. According to the properties of derivation for finite integral, the derivation of $\varphi(t)$ with respect to time t can be presented as

$$\varphi'(t) = (f(d_c(t) + \frac{W}{2}) - f(d_c(t) - \frac{W}{2}))d'_c(t) = -\frac{d'_c(t)}{2\lambda} \left(\frac{A}{l_{Tu}l_{Ru}} \sin \frac{2\pi L_u}{\lambda} - \frac{A}{l_{Tl}l_{Rl}} \sin \frac{2\pi L_l}{\lambda} \right), \quad (6)$$

where $f(x) = \frac{A}{l_T l_R} \sin \frac{2\pi L}{\lambda}$, $l_{Tu} = \sqrt{(l_{To})^2 + (d_c(t) + \frac{W}{2})^2}$ and $l_{Ru} = \sqrt{(l_{Ro})^2 + (d_c(t) + \frac{W}{2})^2}$ are upper diffraction path length related to Tx and Rx, $l_{Tl} = \sqrt{(l_{To})^2 + (d_c(t) - \frac{W}{2})^2}$ and $l_{Rl} = \sqrt{(l_{Ro})^2 + (d_c(t) - \frac{W}{2})^2}$ are lower diffraction path length related to Tx and Rx, and $d'_c(t)$ is the moving speed of the object. $L_u = l_{Tu} + l_{Ru}$ ($L_l = l_{Tl} + l_{Rl}$) is the path length through the upper (lower) boundary of the object. Similarly, the imaginary part of the diffraction signal vector is $\omega(t) = -\frac{1}{2\lambda} \int_{d_c(t)-\frac{W}{2}}^{d_c(t)+\frac{W}{2}} \frac{A}{l_T l_R} \cos \frac{2\pi L}{\lambda} dx$ and its derivation with respect to time t is

$$\omega'(t) = (g(d_c(t) + \frac{W}{2}) - g(d_c(t) - \frac{W}{2}))d'_c(t) = -\frac{d'_c(t)}{2\lambda} \left(\frac{A}{l_{Tu}l_{Ru}} \cos \frac{2\pi L_u}{\lambda} - \frac{A}{l_{Tl}l_{Rl}} \cos \frac{2\pi L_l}{\lambda} \right), \quad (7)$$

where $g(x) = \frac{A}{l_T l_R} \cos \frac{2\pi L}{\lambda}$. Then the sum of the squares of Equation 6 and Equation 7 can be denoted as

$$\varphi'(t)^2 + \omega'(t)^2 = \frac{A^2 d'_c(t)^2}{4\lambda^2} \left(\frac{1}{l_{Tu}l_{Ru}} - \frac{1}{l_{Tl}l_{Rl}} \right)^2 + \frac{A^2 d'_c(t)^2}{\lambda^2 l_{Tu}l_{Ru}l_{Tl}l_{Rl}} \sin^2 \pi \frac{L_u - L_l}{\lambda}. \quad (8)$$

Furthermore, as shown in Figure 9, we can divide the area around transceivers into three regions. When the object moves in the middle region (i.e., region ②) and the object size is smaller than the LoS distance, the term $(\frac{1}{l_{Tu}l_{Ru}} - \frac{1}{l_{Tl}l_{Rl}})^2$ becomes very small in comparison with the second term and the first term of Equation 8 can thus be ignored. When LoS is 2 m, the minimum horizontal range of region ② is 1.6 m. After ignoring the first term, Equation 8 can be simplified as

$$\varphi'(t)^2 + \omega'(t)^2 \approx \frac{A^2 d'_c(t)^2}{\lambda^2 l_{Tu}l_{Ru}l_{Tl}l_{Rl}} \sin^2 \pi \frac{L_u - L_l}{\lambda}. \quad (9)$$

As we focus on measuring the size of a moving object (i.e., the object's speed is not zero, $d'_c(t)^2 \neq 0$), therefore, the singularity appears when $L_u - L_l = \frac{k\lambda}{2}$, $k \in N$. Different widths of objects cause different path length differences. When the path length difference is an integer multiple of the wavelength λ , the singularity appears. Figure 10 shows that when the path length difference introduced by an object is exactly one wavelength, a

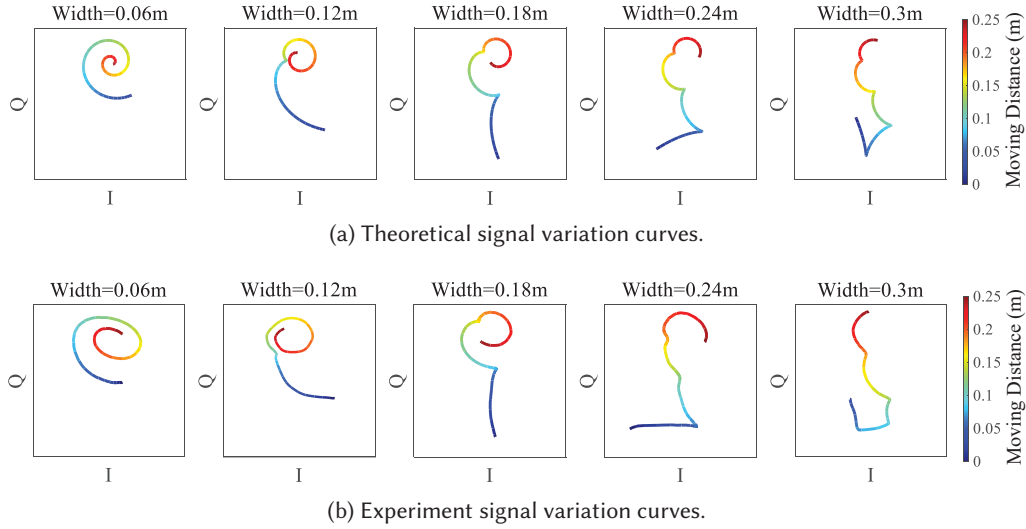


Figure 12. Signal curves on the complex plane when objects with different widths move 0.25 m on the perpendicular bisector of the transmitter-receiver pair with a LoS of 1 m.

singularity appears on the diffraction signal. Note that the relationship between the singularity and the object width applies not only to objects on the perpendicular bisector of the two transceivers, but also to objects located at other positions in the diffraction region.²

Next, we investigate the number of singularities when an object moves away from the LoS path. As shown in Figure 11, when the center of the object is located on the LoS path, the path length difference between the upper boundary and the lower boundary is zero. As the object moves upwards, the path length difference gradually increases. When the path length difference is λ , 2λ ..., singularities occur. If the object moves a fixed distance from the LoS path, based on the path length difference at the ending position, the number of singularities N on the diffraction signal curve during the movement process of the object can be calculated as

$$N = \text{floor}\left(\frac{L_{u_{\text{end}}} - L_{l_{\text{end}}}}{\lambda}\right). \quad (10)$$

From Equation 10, we can observe that the number of singularities is directly related to the path length difference between the upper boundary and lower boundary of the object at the end position, which further depends on four parameters, i.e., end location, signal wavelength, object's width, and LoS path length. Specifically, (i) End location. The further the end location is from the LoS path, the greater the path length difference and the larger the number of singularities. (ii) Signal wavelength. For an object of the same size and end location, the smaller the wavelength, the larger the number of singularities. (iii) Object's width. The wider the object, the larger the difference in path length and accordingly the larger the number of singularities. (iv) LoS path length. As the LoS path length increases, the path length difference decreases and the number of singularities decreases. In our design, we fix the signal wavelength and the end location. We next investigate the effect of object's width and LoS path length on the number of singularities for size measurement.

²The diffraction region is mainly inside the First Fresnel Zone [17]

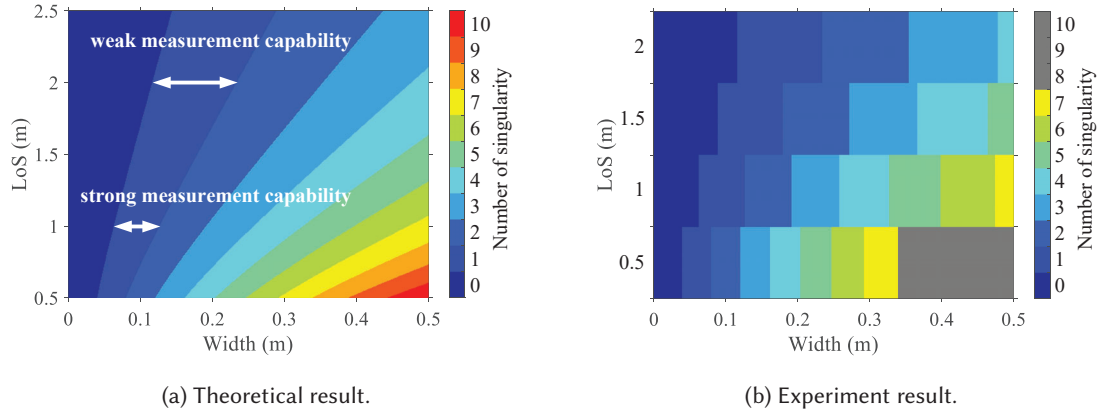


Figure 13. Impact of LoS distance on the number of singularities and measurement capability.

2.4 Guidelines for Size Measurement

Next, we analyze the effect of object width and LoS path length on the number of singularities.

2.4.1 The Relationship between Object Size and the Number of Singularities. We first analyze how object width affects the number of singularities. We consider five different object widths, i.e., 0.06 m, 0.12 m, 0.18 m, 0.24 m and 0.3 m. We let the object move 0.25 m along the perpendicular bisector of the LoS path and the corresponding signals are shown in Figure 12a. We can clearly see that the number of singularities is 0, 1, 2, 3 and 4, respectively for the five object widths. The path length difference of the object at 0.25 m is 0.053 m, 0.106 m, 0.159 m, 0.210 m and 0.260 m, corresponding to 0.94, 1.87, 2.79, 3.69 and 4.57 times the wavelength (0.057 m). So theoretically, the larger the object width, the larger number of singularities, which indicates we can use the number of singularities to estimate the width of the object.

Next, we validate the theoretical relationship with experiments. The experiment setup is identical to that in Section 2.2. We can see that the experiment results in Figure 12b match the theoretical curves well.

2.4.2 The Relationship between the LoS Path Length and the Number of Singularities. Next, we analyze the influence of the distance between transceivers (i.e., the LoS path length) on the number of singularities. Figure 13a presents the theoretical heatmap of the number of singularities for different object widths under different LoS path lengths. We can observe that *when the number of singularities is the same, the larger the LoS, the lower the object width resolution*. This means a larger range of object width will induce the same number of singularities, also indicating a weaker object width measurement capability. For example, when LoS path length is 0.5 m, 10 different object widths within 0~50 cm can be obtained because 10 singularities can be detected with each number of singularities corresponding to one object width. If the LoS path length is increased to 2 m, only four different object widths within 0~50 cm can be obtained.

We now conduct experiment to verify the theoretical relationship between the LoS distance and the number of singularities. We vary the LoS path length from 0.5 m to 2.5 m at a step size of 0.5 m, and count the number of singularities when we increase the object width from 0.1 m to 0.5 m at a step size of 0.01 m. We present the experiment results in Figure 13b. We can see that the experiment results match the theoretical plots very well. When the object is too large (i.e., close to the LoS path length), the majority of the signal power is blocked rather than diffracted, leading to a weak signal-to-noise ratio. Therefore, when the LoS is 0.5 m, only objects with a

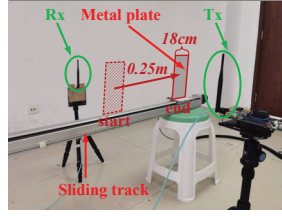


Figure 14. Experiment setup.

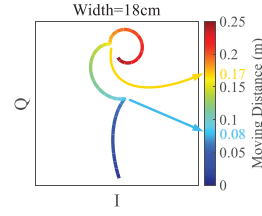


Figure 15. Theoretical signal variation pattern.

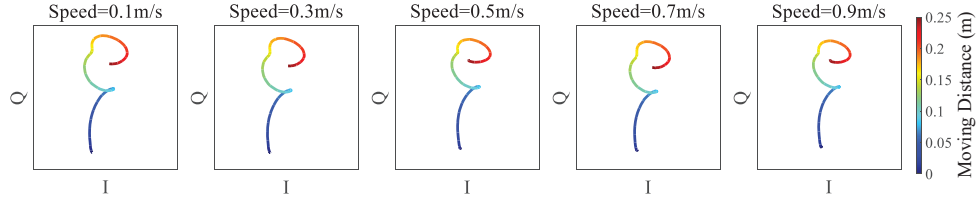


Figure 16. Signal variation patterns when an object moves a distance of 0.25 m at different speeds.

width smaller than 0.34 m can be measured. So if we would like to measure the size of larger objects, we need to place the transmitter and receiver with a larger distance.

2.5 Model Evaluation

In this section, we comprehensively study the effect of target speed, shape, height, and antenna height with both simulation and real-world experiment. The key observations are summarized as follows:

- **Impact of moving speed.** The conveyor belt speed is generally in the range of 10 cm/s to 70 cm/s. For example, the industrial assembly line usually moves at a speed of 10-20 cm/s [2] and an airport baggage conveyor moves at a speed in the range of 40 to 50 cm/s [1]. We first study the effect of target moving speed. A sliding track with a length of 1 m is employed to move the metal plate (i.e., target) at different speeds (from 10 cm/s to 90 cm/s at a step size of 20 cm/s). As shown in Figure 14, we let the metal plate with a size of 18×25 cm move along the perpendicular bisector of the transmitter-receiver pair, starting from $d_c(start) = 0$ (middle point of LoS) and stopping at $d_c(end) = 0.25$ m. The transmitter sends out WiFi packets at a rate of 1000 pkt/s on the 5.32 GHz WiFi band with a channel bandwidth of 20 MHz. The theoretical signal variation pattern is shown in Figure 15. Experiment results in Figure 16 show that two singularities exist on the CSI trajectory at 0.08 m and 0.17 m from the LoS path. These collected CSI trajectories match the theoretical curve (Figure 15) very well.
- **Impact of object shape.** Commonly seen shapes include cube, cuboid, cylinder, and frustum of cone as shown in Figure 17. To study the impact of shape, we select objects of different shapes from everyday life including cube box, cuboid box, can, and cup as shown in Figure 18. The experiment setup is the same as that described in the previous section. The object moves at a speed of 0.1 m/s and the LoS distance is 0.5 m. We can derive the signal trajectory and count the number of singularities theoretically using the LoS plane width (red line in Figure 18) as the theoretical object width. As shown in Table 1, the experiment results and the theoretical results are consistent.
- **Impact of object height.** The height of parcel boxes is generally between 9 cm and 63 cm [3]. We choose parcel boxes of different heights (12 cm, 25 cm, 40 cm and 63 cm) as shown in Figure 19 to explore the

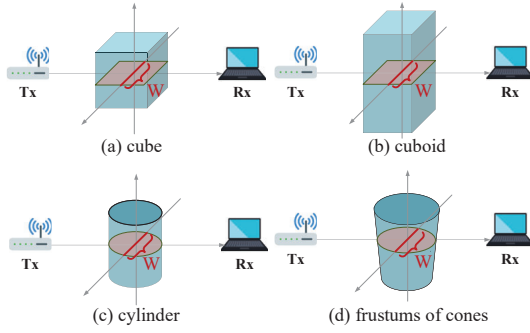


Figure 17. Measuring the width of a target of different shapes.

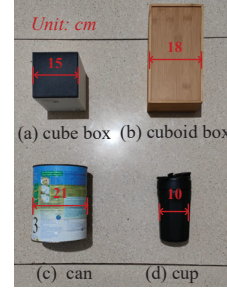


Figure 18. Objects of different shapes.

Table 1. Number of singularities for the four shapes of objects in theory and in experiment.

	cube box	cuboid box	can	cup
Theoretical results	3	4	5	2
Experimental results	3	4	5	2

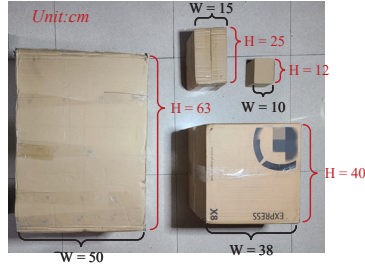


Figure 19. Objects of different heights.

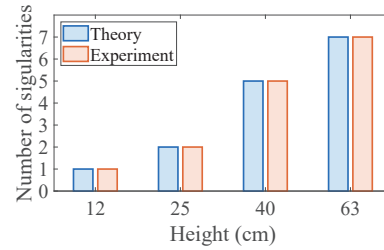


Figure 20. The effect of height on object width measurement.

influence of height on the model. The experiment setting is similar to that described in the previous section. As shown in Figure 20, the number of singularities measured in the experiment matches the theoretical number of singularities calculated using the proposed model. Therefore, we can conclude that the impact of height is limited. Note that when the object size is much larger (e.g., 1-2 m), we need to vary the LoS distance between the transmitter and receiver in order to accommodate the target of a larger size.

- **Impact of antenna height.** The antenna height can be adjusted with respect to the assembly line. To evaluate the effect of antenna height, we fix the position of the metal plate and adjust the antenna height to the following 5 positions as shown in Figure 21: the center of the object blocks the LoS path of the antenna (Figure 21a), the upper edge of the object just blocks the LoS path (Figure 21b), the lower edge of the object just blocks the LoS path (Figure 21c), and the object does not block the LoS path (Figure 21d and e). As the metal plate is 12 cm wide, one singularity exists on the collected CSI trajectory. Table 2 shows that the experiment results match theoretical results well and the effect of antenna height is negligible. However, if the antenna height is too low or too high and the LoS path is not blocked by the object, the

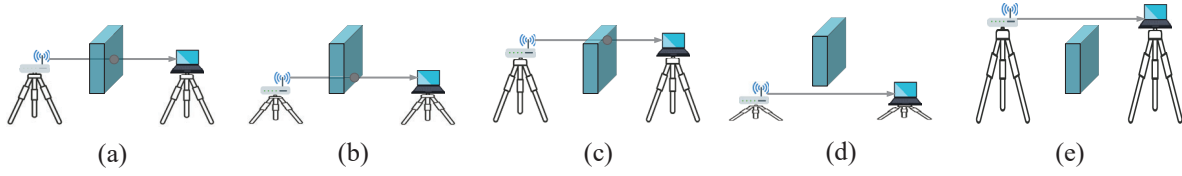


Figure 21. Target size measurement at different antenna heights.

Table 2. The number of singularities at five different antenna heights.

Case (a)	Case (b)	Case (c)	Case (d)	Case(e)
1	1	1	0	0

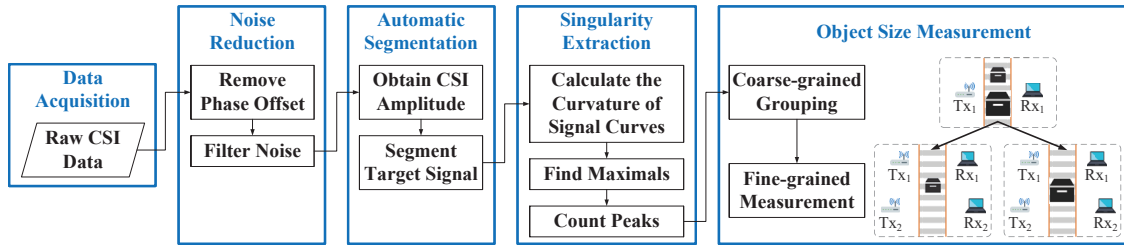


Figure 22. System overview of WiMeasure.

performance degrades. We therefore suggest the users adjust the antenna heights to ensure the LoS path is blocked by the target to achieve accurate size measurements.

3 SYSTEM DESIGN FOR SIZE MEASUREMENT

In this section, guided by the proposed theoretical model, we design WiFi based object size Measurement system (i.e., WiMeasure). Figure 22 presents the system overview diagram which consists of five modules, i.e., data acquisition, noise reduction, automatic segmentation, singularity extraction, and object size measurement. Raw CSI data is collected from multiple pairs of WiFi transceivers and is denoised to remove phase offsets and reduce noise. Afterward, we identify the timestamp when the object passes through the LoS path and segment the CSI data when the object is within the diffraction area. Then the CSI data is employed to calculate the number of singularities. Finally, we combine the results from multiple pairs of WiFi transceivers to obtain accurate object size information. Raw CSI samples are collected from commodity WiFi devices, and the hardware setup will be presented in Section 5. Next, we introduce the design of the remaining four modules.

3.1 Noise Reduction

As shown in Figure 23, when a metal plate passes through the middle of WiFi transceiver pair, the raw CSI readings collected from commodity WiFi devices are too noisy to extract the desired signal patterns induced by object's movement. In order to extract the singularities from the CSI signals for size measurement, we need to denoise the raw CSI data first. Because the transmitter and receiver are not clock-synchronized, phase errors are introduced by the Phase Locked Loop (PLL), Sampling Frequency Offset (SFO) and Packet Boundary Detection (PBD) uncertainty. Since different antennas on the same WiFi card share the same clock, they have the same PLL, SFO, and PBD.

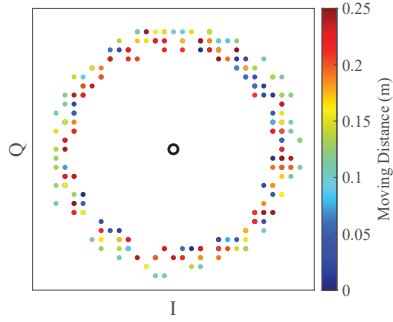


Figure 23. Raw signal on the complex plane.

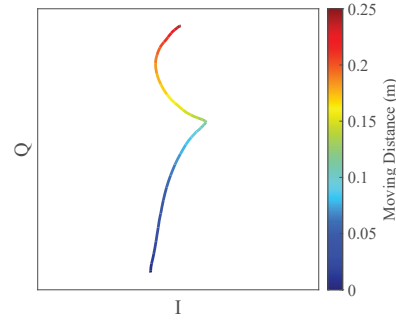


Figure 24. Signal with ratio and filter operations.

This offers us an opportunity to eliminate the influence of random phase offsets. Based on this key observation, we apply the CSI ratio operation on the CSIs collected from two antennas on the same WiFi card to eliminate the random phase offset (θ_0) [55, 56]

$$H_{ratio} = \frac{e^{-i\theta_0} H_1(t)}{e^{-i\theta_0} H_2(t)} = \frac{H_1(t)}{H_2(t)}, \quad (11)$$

where $H_1(t)$ and $H_2(t)$ are the CSIs collected from two antennas on the same WiFi card. According to the property of periodicity protection for complex division, it can be proved that the ratio operation does not affect the occurrence of singularities [31]. Next, a least-square smoothing filter, i.e., Savitzky-Golay filter [40] is applied to further denoise the amplitude noise of resulted CSI ratio. After the filter is applied, the raw CSI gets smoothed as a curve shown in Figure 24, and we can observe a clear signal trajectory over time on the complex I-Q plane for singularity extraction.

3.2 Automatic Segmentation

As the number of singularities is related to the moving distance, to utilize the number of singularities for object width measurement, we need to decide which CSI segment is most suitable for size measurement and use a fixed amount of distance for size measurement. Based on our theoretical analysis and experiment, we want to choose the CSI segment near to LoS path for size measurement because the diffraction effect is stronger when the object is closer to the LoS path. Very interestingly, we can accurately identify the point on the CSI trajectory when an object crosses the LoS, i.e., the center of the object is exactly at the LoS path without any prior knowledge. As shown in Figure 25a, the signal amplitude during the process of crossing the LoS path varies in the shape of “W”. What is more important, the signal variation pattern is symmetrical with respect to the LoS path. We can therefore apply this property of symmetry to identify the point when the middle of the object is at the LoS path as the starting point (i.e., t_{start}). Specifically, we identify the two minima on the “W”-shaped signal and take the average of the two minima time $\frac{t_1+t_2}{2}$ as the starting time t_{start} . After the starting point is determined, we also need to decide the distance range we will use for singularity counting. A larger distance presents us a larger number of singularities. However, when the object is further away from the LoS path, the diffraction effect is also weaker. Based on our experience, we set the distance range as 0.25 m, which means we count the number of singularities when the object moves from the LoS path (t_{start}) to a distance 0.25 m away from the LoS (t_{end}). As the sliding rail speed or the product line belt speed is known and constant, we can easily identify the CSI segment within the t_{start} and t_{end} for size measurement. Figure 25b shows the experiment data, i.e., the CSI amplitude after noise reduction. By applying the above method, we can accurately identify the signal segment corresponding to the object moving 0.25 m from the LoS path.

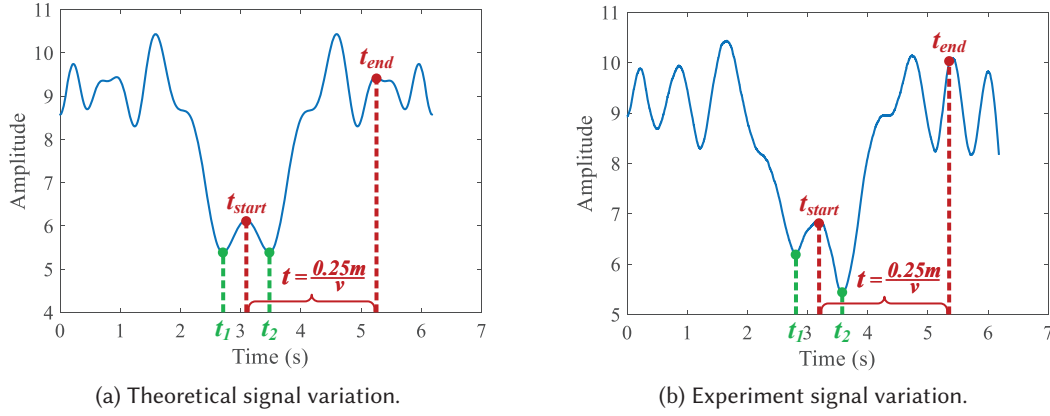


Figure 25. Identify the signal segment for the object that moves 0.25 m.

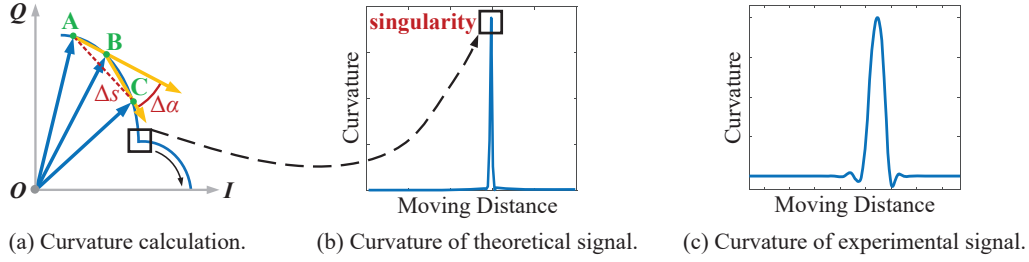


Figure 26. Applying the curvature feature to extract singularities.

3.3 Singularity Extraction

The next step is to extract the number of singularities from the identified CSI segment. From the previous section, we know that there is a sharp direction change but not a sharp power change at the singularity. Therefore, to accurately detect a singularity, the straightforward solution is to find the point where the signal vector direction deviates sharply in time. Mathematically, we use the curvature to describe the speed of direction change. If we know 3 adjacent points on the CSI trajectory (e.g., A, B, C as shown in Figure 26a), we can calculate the curvature of the three points. This curvature information presents us with one advantage for singularity extraction. As shown in Figure 26b, we present the curvature plots for one object moving 0.25 m along the perpendicular bisector of the two transceivers. The curvature value of the singularity is very large and we thus can achieve very robust singularity detection by applying a simple peak detection algorithm.

Now, let us illustrate how to calculate the curvature using three adjacent points on CSI trajectory. The curvature of a curve at a point is the rate of change in the tangential direction. For example, consider three points A, B, C in Figure 26a, the change of tangential angles between A and C is $\Delta\alpha = \text{Angle}(\vec{AB}) - \text{Angle}(\vec{BC})$ and the length of arc AC is Δs . The curvature κ at B is computed by moving A and C infinitely closer to B as

$$\kappa = \lim_{\Delta s \rightarrow 0} \left| \frac{\text{Angle}(\vec{AB}) - \text{Angle}(\vec{BC})}{\Delta s} \right| = \lim_{\Delta s \rightarrow 0} \left| \frac{\Delta\alpha}{\Delta s} \right|. \quad (12)$$



Figure 27. Coarse-grained grouping.

Figure 26b shows the estimated curvature values over time when the object moves. Figure 26c shows the obtained curvature values using real CSI data collected, which match the theoretical curve very well. The curvature peak indicates the singularity, and the number of singularities during the movement can be extracted by counting the number of curvature peaks.

3.4 Object Size Measurement

After extracting the number of singularities, we proceed to measure the object's size. The measurement process consists of two steps, i.e., the coarse-grained size measurement step and the fine-grained size measurement step. The coarse-grained size measurement step coarsely groups target size into a few categories, while the fine-grained size measurement step further determines the exact numerical value of the object size. We employ one transmitter-receiver pair in the coarse-grained measurement step and two transmitter-receiver pairs in the fine-grained measurement step. Both coarse-grained and fine-grained size measurements are useful in industrial applications. For example, coarse-grained size measurement can be used to group boxes of different sizes in logistics, while fine-grained measurements can be used to measure the exact size of products.

3.4.1 Step 1: Coarse-grained size measurement. In coarse-grained size measurement, our goal is to group the target size into a few categories (e.g., 4 cm~8 cm, 8 cm~12 cm, etc.). In Section 2.4, the proposed model shows that a small LoS distance can achieve a finer resolution on size measurement. However, we can not keep reducing the LoS distance as we still need to make sure the LoS distance is larger than the target size in order for the target to move through. Without loss of generality, we choose a LoS distance of 0.5 m as an example to illustrate the concept. As shown in Figure 27, based on the number of singularities, objects can be grouped into five categories ranging from 4 cm to 24 cm with a step size of 4 cm.

3.4.2 Step 2: Fine-grained size measurement. After the coarse-grained size measurement step, i.e., grouping the target size into categories at an accuracy of a few centimeters, we now move to obtain the fine-grained target size at an accuracy of millimeter. In this step, we employ multiple pairs of transceivers for size measurement. Note that in the coarse-grained measurement step, we can determine the coarse size range of an object (e.g., an object has a size in the range of 12 cm to 16 cm). Now, we further use this range information to configure the LoS distance between the WiFi transceiver pairs for fine-grained measurement.

The basic idea is to further divide coarse-grained range bins in Step 1 into more fine-grained range bins. For example, the 12 cm~16 cm range bins is now divided into two smaller range bins (i.e., 12 cm~14 cm and 14 cm~16 cm). To achieve this, we need to carefully design the LoS distance using the properties revealed in Section 2.4. For the sake of simplicity, we divide the large range bin into equal smaller range bins and use the middle value of the smaller range bin as the measured value. As illustrated in Figure 28a, the number of singularities varies with the LoS distance for a given range bin (i.e., 12 cm~16 cm). We first identify the midpoint (i.e., 14 cm) of the range bin and utilize it to select the LoS distance (i.e., 0.66 cm) that generates a different number of singularities in the two smaller range bins (i.e., two singularities in 12 cm~14 cm and three singularities in 14 cm~16 cm). Therefore, if we choose a LoS distance of 0.66 m, when there are two singularities, the width of the system is measured as 13 cm (Figure 28b). When three singularities exist, the object width is measured as 15 cm. Thus, with one pair of transceivers, the maximum error is one-quarter of the object's width range, i.e., 1 cm.

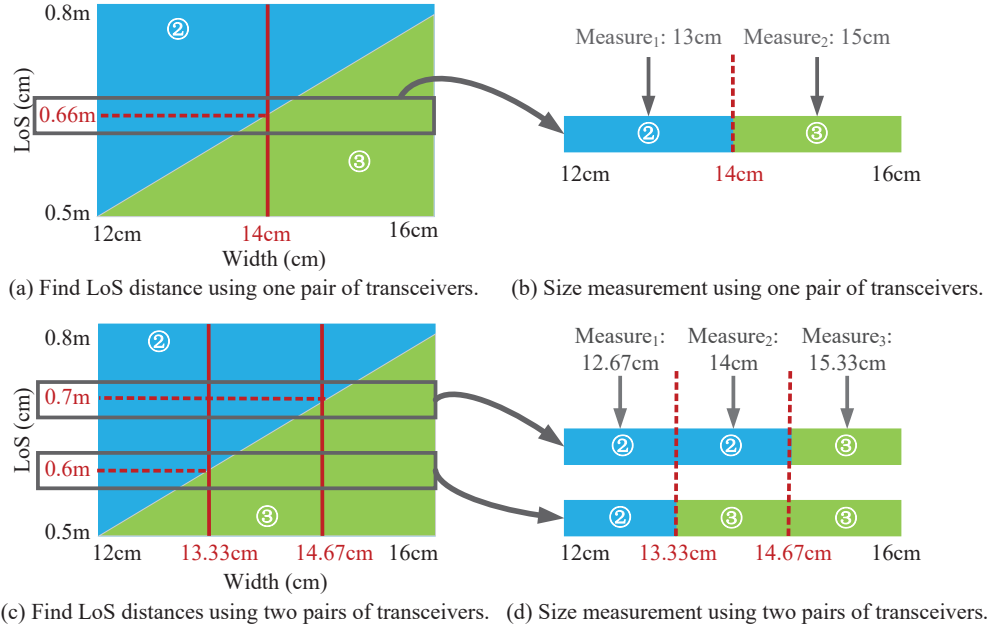


Figure 28. Achieve fine-grained size measurement using one (two) pair(s) of devices.

Similarly, with two pairs of transceivers, we can divide the range bin into three equal smaller range bins as shown in Figure 28d. One transmitter-receiver pair is used to identify the first and second smaller range bins, while a second transmitter-receiver pair is used to identify the second and third smaller range bins. As illustrated in Figure 28c, the breakpoints are 13.33 cm and 14.67 cm, corresponding to a LoS distance of 0.6 m and 0.7 m, respectively. As shown in Figure 28d, when there are two singularities for both 0.6 m and 0.7 m LoS distances, the measured size is 12.67 cm ($\frac{12+13.33}{2}$). If there are two singularities for the 0.7 m LoS distance and three singularities for the 0.6 m LoS distance, the measured size is 14 cm ($\frac{13.33+14.67}{2}$). And when there are three singularities for both LoS distances, the measured size is 15.33 cm ($\frac{14.67+16}{2}$). In this two-transceiver-pair case, we can achieve an error less than 0.66 cm ($\frac{4cm}{2(2+1)}$). By leveraging n pairs of transceivers with n different LoS distances, our system can measure the target width with an error smaller than $\frac{1}{2(n+1)}$ times the coarse width range obtained in Step 1. Theoretically, it is possible to measure the target width within an arbitrarily small range with an infinite number of transmitter-receiver pairs. In this work, we show that with just three transmitter-receiver pairs, we are able to achieve millimeter-level measurement accuracy.

4 SYSTEM IMPLEMENTATION AND APPLICATIONS

4.1 System Implementation

For the implementation of WiMeasure, we employ GigaByte MiniPCs equipped with Intel 5300 WiFi cards as transceivers. The transmitter is configured with one omnidirectional antenna while the receiver is equipped with three omnidirectional antennas capturing three CSI streams. The transmitter is set to injection mode to continuously transmit WiFi packets at a rate of 500 pkts/s. The receiver works in monitor mode to capture WiFi packets from the transmitter and extract CSI streams. To avoid frequency interference, the transmitter-receiver pairs are configured to work on different channels. A Dell laptop with Intel i7 CPU and 16G RAM is connected

Table 3. The size of four standard parcel boxes from Amazon

Object Size Index	Size1	Size2	Size3	Size4
Size (cm)	9	13.5	18	22

Table 4. LoS distance design for fine-grained size measurement.

Pairs of Transceivers	LoS (m)				
	4 cm-8 cm	8 cm-12 cm	12 cm-16 cm	16 cm-20 cm	20 cm-24 cm
1	0.94	0.73	0.66	0.93	0.82
2	0.81, 1.08	0.66, 0.80	0.61, 0.70	0.89, 0.98	0.79, 0.86
3	0.74, 0.94, 1.14	0.62, 0.73, 0.84	0.58, 0.66, 0.73	0.86, 0.93, 1.00	0.77, 0.82, 0.87

to the receivers with routers and processes the CSI readings with Matlab to report the measurement results. In addition, we employ the sliding rail with an accuracy on the scale of sub-millimeter to precisely control the object movement. The transceivers and sliding rail are placed at the same height of 0.65 cm.

4.2 Applications

4.2.1 Coarse-grained size measurement for parcel box classification. In logistics, grouping parcel boxes based on their sizes is critical for allocating appropriate storage space. Table 3 lists the sizes of Amazon’s standard parcel boxes. To distinguish these parcel boxes, coarse-grained size measurement proposed in Section 3.4 is enough. We note that the average dimension difference between adjacent box sizes is about 4 cm. Based on the design proposed in Section 3.4, our system only needs to employ one transmitter-receiver pair with a LoS distance of 0.5 m to distinguish these parcel boxes.

4.2.2 Fine-grained size measurement for daily objects. Fine-grained size measurement is required when designing packing boxes for daily objects such as glasses and cups. To capture target’s fine-grained size, WiMeasure first leverages one transmitter-receiver pair to coarsely classify the objects. Then one/two/three transmitter-receiver pair(s) with carefully designed LoS distances as shown in Table 4 are employed to measure the fine-grained object size.

5 EVALUATION

In this section, the evaluation metric of WiMeasure is first introduced, followed by the overall performance evaluation including coarse-grained size grouping accuracy and fine-grained size measurement error. We also study the effect of factors such as moving speed and material on performance.

5.1 Experiment Setup

5.1.1 Coarse-grained size grouping. We use one pair of transceivers for coarse-grained size grouping. In this experiment, we collect a total of 1500 CSI traces (4 widths \times 5 trajectories \times 5 speeds \times 3 environments \times 5 repetitions). Table 3 presents the side length of 4 commonly used FBA (fulfillment by Amazon) packaging boxes of different sizes. The proposed system is applied to differentiate these boxes. As shown in Figure 27, it becomes clear that these four objects correspond to 2, 3, 4, and 5 singularities when the LoS distance is 0.5m. The number of singularities corresponding to each object is regarded as the true value, and the number of singularities extracted

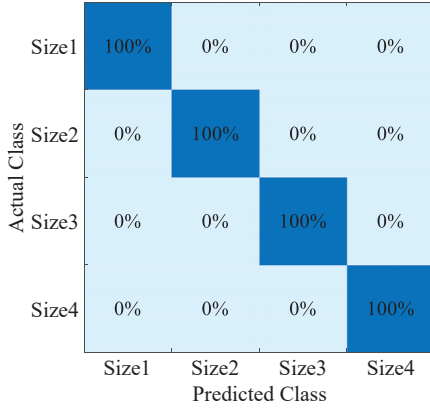


Figure 29. Confusion matrices for coarse-grained object classification.

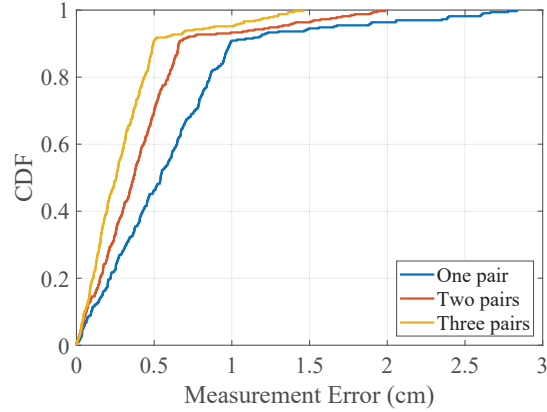


Figure 30. Overall performance for fine-grained size measurement.

from the CSI signal is regarded as the measured value. When the measured number of singularities is consistent with the true value, the grouping is correct. The grouping accuracy is defined as the percentage of correctly grouped cases compared to the total number of cases.

5.1.2 Fine-grained size measurement. Table 4 presents the experiment setting for fine-grained size measurement. We select five different object width ranges to measure: 4 cm to 8 cm, 8 cm to 12 cm, 12 cm to 16 cm, 16 cm to 20 cm, and 20 cm to 24 cm. For each range bin, we measure the objects using 1, 2, and 3 pairs of transceivers. We also evaluate the performance when measuring the size of objects made of different materials such as metal, wood, porcelain, glass, carton, and even fruit. In order to determine the ground truth width of the object, we use a vernier caliper with a measurement accuracy of 0.01 mm. The difference between the measured width and the ground truth width is the width measurement error.

5.2 Overall Performance

As shown in Figure 29, we calculate the accuracy confusion matrix using our coarse-grained grouping system. Although the sizes of the boxes differ only by about 4 cm, we are still able to achieve 100% coarse-grained grouping accuracy. Note that it is possible to differentiate boxes by the human eye when the size difference is big. However, when the size difference is small (e.g., 4 cm in our experiment), the accuracy of manual classification is low.

We further show the performance of fine-grained size measurement error. Figure 30 shows the CDF (cumulative distribution function) of fine-grained measurement errors for all objects using 1, 2, and 3 pairs of transceivers respectively. As can be seen from the figure, when using 1, 2, and 3 pairs of transceivers, the median width measurement error is 0.54 cm, 0.37 cm, and 0.26 cm, respectively. The measurement error is the largest when one pair of transceivers are used, and it decreases as the number of transceivers increases. In addition to being the first work using WiFi signals to measure the size of objects, the proposed system can achieve a high accuracy on the scale of millimeter level.

5.3 Evaluation of System Robustness on Coarse-grained Size Grouping

Next, we evaluate the impact of environment, moving speed and trajectory on the performance of coarse-grained grouping. When evaluating a specific factor, we keep the other impact factors unchanged.

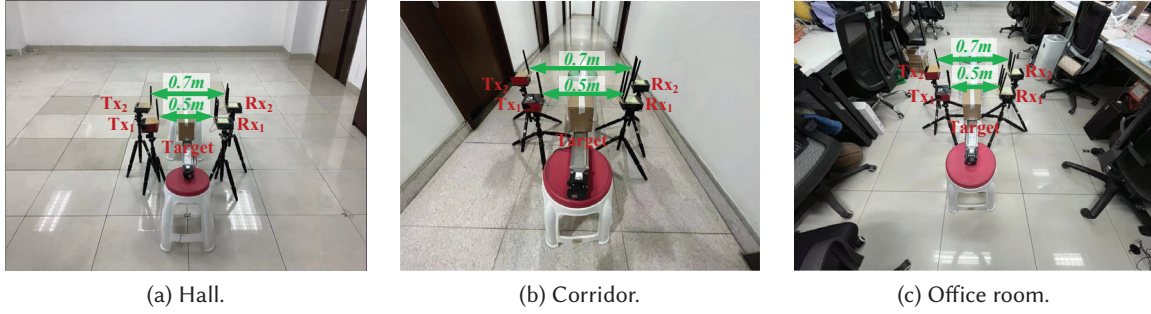


Figure 31. Experiment setup in three environments.

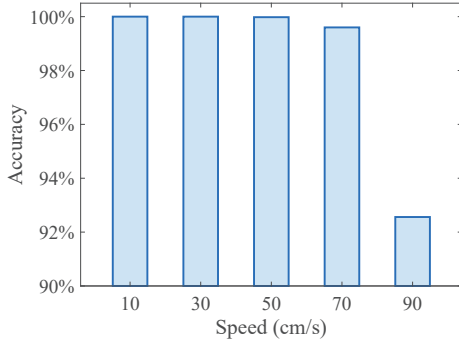


Figure 32. Impact of moving speed on grouping accuracy.

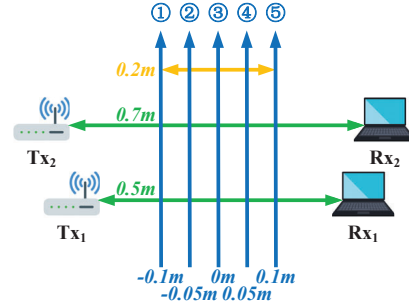


Figure 33. The experiment setup with the five moving trajectories marked.

5.3.1 Impact of environment. We conduct experiments in three different environments, i.e., a large hall with little multipath (Figure 31a), a corridor with some multipath (Figure 31b) and a graduate student office with rich multipath (Figure 31c). The object moving speed is 50 cm/s. We demonstrate that our system can achieve 100% grouping accuracy in three different environments. We can see that multipath has very little effect on performance. This is because we use curvature to detect singularities, and the curvature information is not related to signals reflected from static objects such as walls, ground, etc. As long as there are no moving targets, multipath induced by static objects has little effect on the performance.

5.3.2 Impact of moving speed. Different belts move at different speeds. A conveyor belt at airport security generally moves at a speed of 22 cm/s and an airport baggage conveyor belt typically moves at a speed of 40 cm/s to 50 cm/s. The factory conveyor belts move at a speed in the range of 10 cm/s to 70 cm/s. In this experiment, we vary the object moving speed from 10 cm/s to 90 cm/s at a step size of 20 cm/s to see the effect of speed on size grouping accuracy. The results are shown in Figure 32. We can see that a slower moving speed does lead to higher accuracy. We observe a performance degradation (99.6% to 92.6%) when the speed is increased to 90 cm/s. This is because when the speed is larger, the number of CSI samples when the object moves for a fixed distance is less and the sample rate of 500 pkt/s is insufficient to accurately detect the singularity. Therefore, if the belt speed is higher than 0.7 m/s, we suggest increasing the packet rate in order to maintain high grouping accuracy.



Figure 34. Five objects of different sizes.

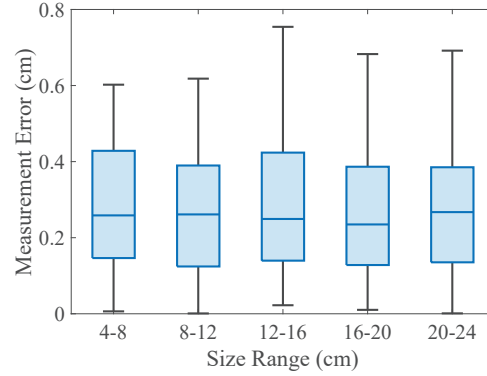


Figure 35. Impact of object width on the measurement error.

5.3.3 Impact of moving trajectory. On the assembly line, the object may not be placed exactly in the middle of the belt. The object can have an offset with respect to the middle line. We now conduct experiment to see the effect of different object trajectories with respect to the middle line as shown in Figure 33. We consider five trajectories, i.e., one in the middle, two with a deviation of 5 cm, and two with a deviation of 10 cm. We find that a grouping accuracy of 100% can be achieved under all five trajectories and the proposed system is robust against middle-line deviations. This is because the signal path length changes very little and the number of singularities is not affected. If the object deviates too much from the middle line, the deviation may result in a change in the number of singular points counted, causing measurement errors.

5.4 Evaluation of System Robustness on Fine-grained Size Measurements

Now, we evaluate the effect of object width, object thickness and object material on fine-grained size measurements. In the end, we showcase the performance of the proposed system when we apply it to measure the size of apples. Apples are usually grouped based on the size for pricing.

5.4.1 Impact of object width. In this paper, we select 22 objects of different sizes that are common in everyday life for fine-grained size measurement. The size of the objects falls in the range of 4 cm to 24 cm. Five of these objects are shown in Figure 34, including a relatively small toolbox, a can, a medium-sized phone, as well as a relatively large tablet PC and a vacuum cup. As depicted in Figure 35, the object size has no obvious impact on the measurement error. An accuracy between 0.2 cm and 0.3 cm can always be achieved.

5.4.2 Impact of object material. To assess the impact of material on measurement error, we chose five commonly-seen materials in our daily life, i.e., metal, glass, plastic, ceramics, and apple as shown in Figure 36. We repeat each experiment five times. As shown in Figure 37, the mean measurement error (0.16 cm) for the metal object is the smallest. The mean errors for wood, porcelain, glass and fruit are 0.19 cm, 0.19 cm, 0.24 cm and 0.29 cm, respectively. The largest mean error (0.32 cm) occurs with carton. This is because the diffraction effect is strongest with metal while carton can absorb a lot of signal power.

5.4.3 Impact of object thickness. The thickness of most daily objects is less than 21.8 cm [42]. To study the effect of object thickness on measurement accuracy, we select five objects with a thickness of 5 cm, 10 cm, 15 cm, 20 cm, and 25 cm respectively. As we can see in Figure 38, the median measurement errors under different object thicknesses are always less than 0.32 cm and we do not observe an obvious performance difference. This result



Figure 36. Six objects of different material.

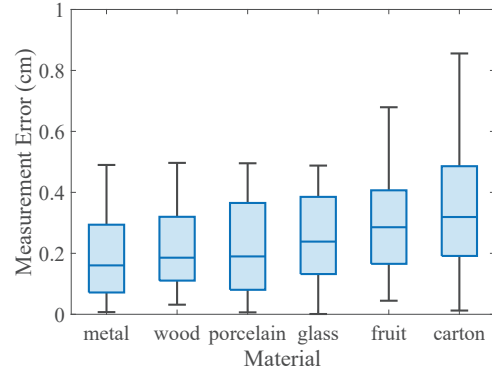


Figure 37. Impact of object material on the measurement error.

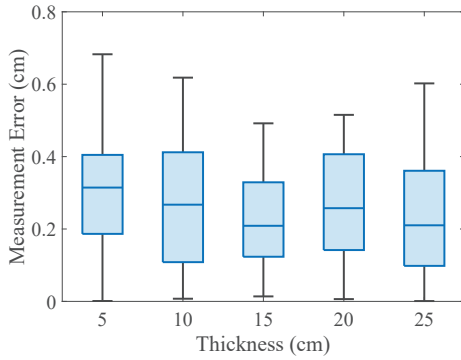


Figure 38. Impact of object thickness on the measurement error.

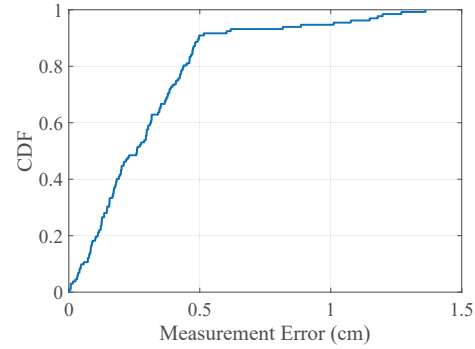


Figure 39. Apple size measurement error.

also matches the theoretical findings reported in a recent work [18] that the object thickness does not affect the signal diffraction pattern when the object is near the LoS path. This result demonstrates the robustness of the proposed system under different target thicknesses.

5.4.4 Apple size measurement. Finally, we chose one commonly-seen object, i.e., apple as our target to show the performance of the proposed system. Apple is not composed of one particular material and can be irregular in shape. During the measurement process, we measure the size of 10 randomly selected apples with a diameter ranging from 6.2 cm to 9.8 cm, using three pairs of transceivers. We employ the proposed system to measure the length of the middle part of the apple. The ground truth is measured using a vernier caliper with an accuracy of 0.01 mm. Figure 39 shows the CDFs of measurement errors. We can see that even for irregular-shaped apples, a low median error of 0.29 cm can still be achieved.

6 RELATED WORK

This chapter introduces the most related literature. We first introduce contactless target imaging and size measurement using high-frequency signals, followed by WiFi-based contactless sensing applications, and finally WiFi-based sensing theories.

6.1 Target Imaging and Size Measurement Using High-frequency Signals

The research for imaging using wireless technologies started in the late 70's [11, 12]. Various approaches ranging from millimeter waves radar [19, 41, 47, 53], terahertz radar [7–9, 13], to laser radar [21, 22, 27, 57, 63] have been explored for imaging and size measurement. The fundamental principle behind size measurement is to capture the point clouds of the target by projecting narrow-beam signals at the target and obtaining accurate time information of the reflection point. To form narrow-beam signals, high frequency and large antenna array are required. To obtain accurate time information, large bandwidth is required. Low-frequency signals (e.g., 2.4 GHz or 5 GHz WiFi signal), however, are limited by the narrow bandwidths (below 160 MHz) and wide beamwidth, making them difficult to be utilized for imaging or size measurement.

6.2 WiFi-Based Contactless Sensing Applications

Although low-frequency signals, such as WiFi, are not suitable for imaging, they are widely used in communication and sensing. WiFi CSI samples contain signal variation information which can be utilized to infer target contexts for sensing. A large range of sensing applications have been realized with WiFi signals. For example, WiFi signals were utilized to identify gestures [5, 14, 15, 33, 48, 61] and daily activities [23, 36, 59], providing us unique opportunities to design novel human-computer interaction methods for smart home automation. WiFi-based contactless respiration monitoring made non-invasive long-term healthcare monitoring possible [29, 30, 43, 45, 54, 55]. Other works also demonstrated the ability of utilizing WiFi signals to extract target information such as location, direction and range [24–26, 32, 49, 50]. However, there is no existing system that is capable of measuring object size using WiFi signals without a need of training.

6.3 WiFi Sensing Theories

In the last few years, besides novel sensing applications, significant progress has also been made in developing theories such as models and metrics to quantify the performance of WiFi sensing. When a target moves near the transceivers, diffraction dominates and when the target is away from the transceivers, reflection dominates. The pioneer work leveraging Fresnel reflection model for human activity sensing [43, 50] was proposed in 2016. While Wu et al. [50] utilized the Fresnel reflection model to detect human walking direction, Wang et al. [43] successfully applied the Fresnel reflection model for human respiration sensing. Additionally, Niu et al. [32] developed the Doppler velocity model to achieve highly accurate human trajectory tracking. The Fresnel diffraction model was introduced first by Rampa et al. for WiFi-based passive localization [28, 39]. The Fresnel diffraction model was further exploited by Wang et al. [44] to push the localization accuracy to 0.5 m using WiFi CSI when the target is within the First Fresnel Zone. Zhang et al. [60] first modeled the Fresnel diffraction effect for human respiration sensing. Zhang et al. [59] also proposed a diffraction model to quantify the relationship between signal variations and target motions for human activity recognition. Different from existing works, the proposed system is the first one achieving fine-grained size measurement using WiFi signals.

7 DISCUSSION AND LIMITATION

Interference from surrounding people. People walking around bring in interference for size measurement. We observe that the interference induced by surrounding people's movements is limited. This is because the majority

of the signal power is concentrated in the first Fresnel zone near the LoS path. Therefore, the interference power outside of the first Fresnel zone is much smaller compared to the diffraction power utilized for size measurement.

Static object. It is difficult for the proposed system to measure the size of a static object due to its low central frequency and small bandwidth. In our work, we present a new modality to achieve accurate object size measurement using WiFi signals. As long as an object moves near the LoS line, the object size can be obtained using low-frequency, narrow-bandwidth signals such as WiFi.

Achieving fine-grained size measurement using just one pair of WiFi transceivers. The proposed system does not require a large bandwidth to work. The ordinary WiFi signal with a 20 MHz channel works well. Based on Equation 10, we know that different frequencies also lead to different numbers of singularities. Therefore, one potential solution to remove the need of multiple WiFi transceiver pairs is to frequency hop to different channels and create virtual antennas. In this way, we can achieve fine-grained size measurement with just one pair of WiFi transceivers.

Target size limit. The target size can not be too small or too big. For example, when the target has a size of 0.5 cm which is much smaller than the signal wavelength (i.e., 5.7 cm), our system does not work well. This is because the proposed system relies on the diffraction effect to work and when the target size is much smaller than the signal wavelength, the diffraction effect becomes too weak to be utilized for size measurement. On the other hand, the size of the target can not be too big. For example, if the LoS path length is 0.5 m, we do observe a performance degradation when the target size is larger than 0.3 m. This is because when the target is relatively large with respect to the LoS path length, blockage dominates and the diffraction effect is also reduced. In order to measure the size of a larger target, we need to deploy the transmitter and receiver at a larger distance.

8 CONCLUSION

In this work, for the first time, we demonstrate that it is possible to accurately measure an object's size using low-frequency narrow-bandwidth WiFi signals. A novel theoretical model is proposed to characterize the quantitative relationship between the number of singularities on WiFi CSI signals and the object's size. Guided by the model, we design and implement a size measurement system on commodity WiFi devices. The proposed system is able to achieve a surprisingly high accuracy (i.e., 2.6 mm) and is robust against environment, material and speed diversities. This work explores an important missing piece of wireless sensing and builds the theoretical foundation for size measurement with low-frequency signals. The proposed method can be applied to other wireless signals such as RFID and LoRa to enable new applications.

ACKNOWLEDGMENTS

This research is supported by NSFC A3 Project 62061146001, PKU-NTU Collaboration Project, and China Postdoctoral Science Foundation (No. 2021TQ0048).

REFERENCES

- [1] 2011. Latest requirements for baggage transfer devices at airports. <https://www.ccaonline.cn/xxcj/552272.html>.
- [2] 2018. Design and control of assembly line speed. <https://www.wxmcdd.com/mc/baike/475.html>.
- [3] 2021. Amazon FBA Maximum Box Size – Explained. <https://projectfba.com/amazon-fba-maximum-box-size/>.
- [4] Heba Abdelnasser, Moustafa Youssef, and Khaled A. Harras. 2015. WiGest: A ubiquitous WiFi-based gesture recognition system. In *2015 IEEE Conference on Computer Communications (INFOCOM)*. IEEE, New York, NY, USA, 1472–1480. <https://doi.org/10.1109/INFOCOM.2015.7218525>
- [5] Kamran Ali, Alex X. Liu, Wei Wang, and Muhammad Shahzad. 2015. Keystroke Recognition Using WiFi Signals. In *Proceedings of the 21st Annual International Conference on Mobile Computing and Networking (Paris, France) (MobiCom '15)*. Association for Computing Machinery, New York, NY, USA, 90–102. <https://doi.org/10.1145/2789168.2790109>
- [6] Max Born. 1980. Principles of optics - electromagnetic theory of propagation, interference and diffraction of light (7. ed.).

- [7] K. B. Cooper, R. J. Dengler, G. Chattopadhyay, E. Schlecht, J. Gill, A. Skalare, I. Mehdi, and P. H. Siegel. 2008. A High-Resolution Imaging Radar at 580 GHz. *IEEE Microwave and Wireless Components Letters* 18, 1 (2008), 64–66. <https://doi.org/10.1109/LMWC.2007.912049>
- [8] Ken B. Cooper, Robert J. Dengler, Nuria Llombart, Tomas Bryllert, Goutam Chattopadhyay, Erich Schlecht, John Gill, Choonsup Lee, Anders Skalare, Imran Mehdi, and Peter H. Siegel. 2008. Penetrating 3-D Imaging at 4- and 25-m Range Using a Submillimeter-Wave Radar. *IEEE Transactions on Microwave Theory and Techniques* 56, 12 (2008), 2771–2778. <https://doi.org/10.1109/TMTT.2008.2007081>
- [9] Ken B. Cooper, Robert J. Dengler, Nuria Llombart, Bertrand Thomas, Goutam Chattopadhyay, and Peter H. Siegel. 2011. THz Imaging Radar for Standoff Personnel Screening. *IEEE Transactions on Terahertz Science and Technology* 1, 1 (2011), 169–182. <https://doi.org/10.1109/TTHZ.2011.2159556>
- [10] Irfan C Engin, Norbert H Maerz, Kenneth J Boyko, and Robert Reals. 2020. Practical measurement of size distribution of blasted rocks using LiDAR scan data. *Rock Mechanics and Rock Engineering* 53 (2020), 4653–4671.
- [11] N.H. Farhat and W.R. Guard. 1971. Millimeter wave holographic imaging of concealed weapons. *Proc. IEEE* 59, 9 (1971), 1383–1384. <https://doi.org/10.1109/PROC.1971.8441>
- [12] B.R. Feingold and B.J. Levin. 1970. Millimeter Wave Imaging. In *G-MTT 1970 International Microwave Symposium*. 126–130. <https://doi.org/10.1109/GMTT.1970.1122786>
- [13] Fabian Friederich, Wolff von Spiegel, Maris Bauer, Fanzhen Meng, Mark D. Thomson, Sebastian Boppel, Alvydas Lisauskas, Bernd Hils, Viktor Krozer, Andreas Keil, Torsten Löffler, Ralf Henneberger, Anna Katharina Huhn, Gunnar Spickermann, Peter Haring Bolivar, and Hartmut G. Roskos. 2011. THz Active Imaging Systems With Real-Time Capabilities. *IEEE Transactions on Terahertz Science and Technology* 1, 1 (2011), 183–200. <https://doi.org/10.1109/TTHZ.2011.2159559>
- [14] Ruiyang Gao, Wenwei Li, Yaxiong Xie, Enze Yi, Leye Wang, Dan Wu, and Daqing Zhang. 2022. Towards Robust Gesture Recognition by Characterizing the Sensing Quality of WiFi Signals. 6, 1, Article 11 (March 2022), 26 pages. <https://doi.org/10.1145/3517241>
- [15] Ruiyang Gao, Mi Zhang, Jie Zhang, Yang Li, Enze Yi, Dan Wu, Leye Wang, and Daqing Zhang. 2021. Towards Position-Independent Sensing for Gesture Recognition with Wi-Fi. *Proc. ACM Interact. Mob. Wearable Ubiquitous Technol.* 5, 2, Article 61 (June 2021), 28 pages. <https://doi.org/10.1145/3463504>
- [16] Ron Goldman. 2005. Curvature formulas for implicit curves and surfaces. *Computer Aided Geometric Design* 22, 7 (2005), 632–658. <https://doi.org/10.1016/j.cagd.2005.06.005> Geometric Modelling and Differential Geometry.
- [17] Andrea Goldsmith. 2005. *Wireless communications*. Cambridge university press.
- [18] Mojtaba Golshani and Mostafa Motamedifar. 2019. Impact of aperture thickness on a Fraunhofer diffraction pattern. *Journal of Optics* 21, 4 (mar 2019), 045605. <https://doi.org/10.1088/2040-8986/ab08cb>
- [19] Junfeng Guan, Sohrab Madani, Suraj Jog, Saurabh Gupta, and Haitham Hassanieh. 2020. Through Fog High-Resolution Imaging Using Millimeter Wave Radar. In *2020 IEEE/CVF Conference on Computer Vision and Pattern Recognition (CVPR)*. 11461–11470. <https://doi.org/10.1109/CVPR42600.2020.01148>
- [20] Wenfeng He, Kaishun Wu, Yongpan Zou, and Zhong Ming. 2015. WiG: WiFi-Based Gesture Recognition System. In *2015 24th International Conference on Computer Communication and Networks (ICCCN)*. IEEE, New York, NY, USA, 1–7. <https://doi.org/10.1109/ICCCN.2015.7288485>
- [21] Wolfgang Hess, Damon Kohler, Holger Rapp, and Daniel Andor. 2016. Real-time loop closure in 2D LIDAR SLAM. In *2016 IEEE International Conference on Robotics and Automation (ICRA)*. 1271–1278. <https://doi.org/10.1109/ICRA.2016.7487258>
- [22] Alex H. Lang, Sourabh Vora, Holger Caesar, Lubing Zhou, Jiong Yang, and Oscar Beijbom. 2019. PointPillars: Fast Encoders for Object Detection From Point Clouds. In *2019 IEEE/CVF Conference on Computer Vision and Pattern Recognition (CVPR)*. 12689–12697. <https://doi.org/10.1109/CVPR.2019.01298>
- [23] Shengjie Li, Xiang Li, Qin Lv, Guiyu Tian, and Daqing Zhang. 2018. WiFit: Ubiquitous Bodyweight Exercise Monitoring with Commodity Wi-Fi Devices. In *2018 IEEE SmartWorld, Ubiquitous Intelligence & Computing, Advanced & Trusted Computing, Scalable Computing & Communications, Cloud & Big Data Computing, Internet of People and Smart City Innovation (SmartWorld/SCALCOM/UIC/ATC/CBDCOM/IOP/SCI)*. 530–537. <https://doi.org/10.1109/SmartWorld.2018.00114>
- [24] Shengjie Li, Zhaopeng Liu, Yue Zhang, Qin Lv, Xiaopeng Niu, Leye Wang, and Daqing Zhang. 2020. WiBorder: Precise Wi-Fi Based Boundary Sensing via Through-Wall Discrimination. *Proc. ACM Interact. Mob. Wearable Ubiquitous Technol.* 4, 3, Article 89 (Sept. 2020), 30 pages. <https://doi.org/10.1145/3411834>
- [25] Xiang Li, Shengjie Li, Daqing Zhang, Jie Xiong, Yasha Wang, and Hong Mei. 2016. Dynamic-MUSIC: Accurate Device-Free Indoor Localization. In *Proceedings of the 2016 ACM International Joint Conference on Pervasive and Ubiquitous Computing (Heidelberg, Germany) (UbiComp '16)*. Association for Computing Machinery, New York, NY, USA, 196–207. <https://doi.org/10.1145/2971648.2971665>
- [26] Xiang Li, Daqing Zhang, Qin Lv, Jie Xiong, Shengjie Li, Yue Zhang, and Hong Mei. 2017. IndoTrack: Device-Free Indoor Human Tracking with Commodity Wi-Fi. *Proc. ACM Interact. Mob. Wearable Ubiquitous Technol.* 1, 3, Article 72 (Sept. 2017), 22 pages. <https://doi.org/10.1145/3130940>
- [27] Yanchao Li, Yanling Yang, Xuesong Xia, Long Gao, Haifang Cong, and Chunhui Wang. 2009. The method for dual-beam laser heterodyne ultra-precision measurement of the glass thickness. In *2009 Conference on Lasers & Electro Optics & The Pacific Rim Conference on Lasers and Electro-Optics*. 1–2. <https://doi.org/10.1109/CLEOPR.2009.5292079>

- [28] Chen Liu, Dingyi Fang, Zhe Yang, Hongbo Jiang, Xiaojiang Chen, Wei Wang, Tianzhang Xing, and Lin Cai. 2016. RSS Distribution-Based Passive Localization and Its Application in Sensor Networks. *IEEE Transactions on Wireless Communications* 15, 4 (2016), 2883–2895. <https://doi.org/10.1109/TWC.2015.2512861>
- [29] Jinyi Liu, Youwei Zeng, Tao Gu, Leye Wang, and Daqing Zhang. 2021. WiPhone: Smartphone-Based Respiration Monitoring Using Ambient Reflected WiFi Signals. 5, 1, Article 23 (March 2021), 19 pages. <https://doi.org/10.1145/3448092>
- [30] Xuefeng Liu, Jiannong Cao, Shaojie Tang, and Jiaqi Wen. 2014. Wi-Sleep: Contactless Sleep Monitoring via WiFi Signals. In *2014 IEEE Real-Time Systems Symposium*. IEEE, New York, NY, USA, 346–355. <https://doi.org/10.1109/RTSS.2014.30>
- [31] Tristan Needham. 1997. *Visual complex analysis*. Oxford University Press.
- [32] Kai Niu, Xuanchi Wang, Fusang Zhang, Rong Zheng, Zhiyun Yao, and Daqing Zhang. 2022. Rethinking Doppler Effect for Accurate Velocity Estimation With Commodity WiFi Devices. *IEEE Journal on Selected Areas in Communications* 40, 7 (2022), 2164–2178. <https://doi.org/10.1109/JSAC.2022.3155523>
- [33] Kai Niu, Fusang Zhang, Yuhang Jiang, Jie Xiong, Qin Lv, Youwei Zeng, and Daqing Zhang. 2019. WiMorse: A Contactless Morse Code Text Input System Using Ambient WiFi Signals. *IEEE Internet of Things Journal* 6, 6 (Dec 2019), 9993–10008. <https://doi.org/10.1109/JIOT.2019.2934904>
- [34] Kai Niu, Fusang Zhang, Xuanchi Wang, Qin Lv, Haitong Luo, and Daqing Zhang. 2022. Understanding WiFi Signal Frequency Features for Position-Independent Gesture Sensing. *IEEE Transactions on Mobile Computing* 21, 11 (2022), 4156–4171. <https://doi.org/10.1109/TMC.2021.3063135>
- [35] Kai Niu, Fusang Zhang, Jie Xiong, Xiang Li, Enze Yi, and Daqing Zhang. 2018. Boosting Fine-Grained Activity Sensing by Embracing Wireless Multipath Effects. In *Proceedings of the 14th International Conference on Emerging Networking EXperiments and Technologies (Heraklion, Greece) (CoNEXT '18)*. Association for Computing Machinery, New York, NY, USA, 139–151. <https://doi.org/10.1145/3281411.3281425>
- [36] Xiaopeng Niu, Shengjie Li, Yue Zhang, Zhaopeng Liu, Dan Wu, Rahul C. Shah, Cagri Tanriover, Hong Lu, and Daqing Zhang. 2021. WiMonitor: Continuous Long-Term Human Vitality Monitoring Using Commodity Wi-Fi Devices. *Sensors* 21, 3 (2021). <https://www.mdpi.com/1424-8220/21/3/751>
- [37] Kun Qian, Chenshu Wu, Zheng Yang, Yunhao Liu, and Kyle Jamieson. 2017. Widar: Decimeter-Level Passive Tracking via Velocity Monitoring with Commodity Wi-Fi. In *Proceedings of the 18th ACM International Symposium on Mobile Ad Hoc Networking and Computing (Chennai, India) (MobiHoc '17)*. Association for Computing Machinery, New York, NY, USA, Article 6, 10 pages. <https://doi.org/10.1145/3084041.3084067>
- [38] Kun Qian, Chenshu Wu, Yi Zhang, Guidong Zhang, Zheng Yang, and Yunhao Liu. 2018. Widar2.0: Passive Human Tracking with a Single Wi-Fi Link. In *Proceedings of the 16th Annual International Conference on Mobile Systems, Applications, and Services (Munich, Germany) (MobiSys '18)*. Association for Computing Machinery, New York, NY, USA, 350–361. <https://doi.org/10.1145/3210240.3210314>
- [39] Vittorio Rampa, Stefano Savazzi, Monica Nicoli, and Michele D'Amico. 2015. Physical Modeling and Performance Bounds for Device-free Localization Systems. *IEEE Signal Processing Letters* 22, 11 (2015), 1864–1868. <https://doi.org/10.1109/LSP.2015.2438176>
- [40] Ronald W Schafer. 2011. What is a Savitzky-Golay filter? [lecture notes]. *IEEE Signal processing magazine* 28, 4 (2011), 111–117.
- [41] David M. Sheen, Douglas L. McMakin, and Thomas E. Hall. 2007. Near Field Imaging at Microwave and Millimeter Wave Frequencies. In *2007 IEEE/MTT-S International Microwave Symposium*. 1693–1696. <https://doi.org/10.1109/MWSYM.2007.380033>
- [42] Huirong Wang. 2020. *Decision on Sizes of the Fast-Moving Consumer Goods Delivery Boxes for On-line Retailers*. Master's thesis. Chang'an University. <https://doi.org/10.26976/d.cnki.gchau.2020.001516>
- [43] Hao Wang, Daqing Zhang, Junyi Ma, Yasha Wang, Yuxiang Wang, Dan Wu, Tao Gu, and Bing Xie. 2016. Human Respiration Detection with Commodity Wifi Devices: Do User Location and Body Orientation Matter?. In *Proceedings of the 2016 ACM International Joint Conference on Pervasive and Ubiquitous Computing (Heidelberg, Germany) (UbiComp '16)*. Association for Computing Machinery, New York, NY, USA, 25–36. <https://doi.org/10.1145/2971648.2971744>
- [44] Ju Wang, Hongbo Jiang, Jie Xiong, Kyle Jamieson, Xiaojiang Chen, Dingyi Fang, and Binbin Xie. 2016. LiFS: Low Human-Effort, Device-Free Localization with Fine-Grained Subcarrier Information. In *Proceedings of the 22nd Annual International Conference on Mobile Computing and Networking (New York City, New York) (MobiCom '16)*. Association for Computing Machinery, New York, NY, USA, 243–256. <https://doi.org/10.1145/2973750.2973776>
- [45] Xuanchi Wang, Kai Niu, Jie Xiong, Bochong Qian, Zhiyun Yao, Tairong Lou, and Daqing Zhang. 2022. Placement Matters: Understanding the Effects of Device Placement for WiFi Sensing. *Proc. ACM Interact. Mob. Wearable Ubiquitous Technol.* 6, 1, Article 32 (March 2022), 25 pages. <https://doi.org/10.1145/3517237>
- [46] Xuyu Wang, Chao Yang, and Shiwen Mao. 2017. PhaseBeat: Exploiting CSI Phase Data for Vital Sign Monitoring with Commodity WiFi Devices. In *2017 IEEE 37th International Conference on Distributed Computing Systems (ICDCS)*. IEEE, New York, NY, USA, 1230–1239. <https://doi.org/10.1109/ICDCS.2017.206>
- [47] Claire M. Watts, Patrick Lancaster, Andreas Pedross-Engel, Joshua R. Smith, and Matthew S. Reynolds. 2016. 2D and 3D millimeter-wave synthetic aperture radar imaging on a PR2 platform. In *2016 IEEE/RSJ International Conference on Intelligent Robots and Systems (IROS)*. 4304–4310. <https://doi.org/10.1109/IROS.2016.7759633>

- [48] Dan Wu, Ruiyang Gao, Youwei Zeng, Jinyi Liu, Leye Wang, Tao Gu, and Daqing Zhang. 2020. FingerDraw: Sub-Wavelength Level Finger Motion Tracking with WiFi Signals. *Proc. ACM Interact. Mob. Wearable Ubiquitous Technol.* 4, 1, Article 31 (March 2020), 27 pages. <https://doi.org/10.1145/3380981>
- [49] Dan Wu, Youwei Zeng, Ruiyang Gao, Shenjie Li, Yang Li, Rahul C. Shah, Hong Lu, and Daqing Zhang. 2023. WiTraj: Robust Indoor Motion Tracking With WiFi Signals. *IEEE Transactions on Mobile Computing* 22, 5 (2023), 3062–3078. <https://doi.org/10.1109/TMC.2021.3133114>
- [50] Dan Wu, Daqing Zhang, Chenren Xu, Yasha Wang, and Hao Wang. 2016. WiDir: Walking Direction Estimation Using Wireless Signals. In *Proceedings of the 2016 ACM International Joint Conference on Pervasive and Ubiquitous Computing* (Heidelberg, Germany) (*UbiComp '16*). Association for Computing Machinery, New York, NY, USA, 351–362. <https://doi.org/10.1145/2971648.2971658>
- [51] Rong Xiang, Wenhui He, Xinna Zhang, Dong Wang, and Yuekang Shan. 2018. Size measurement based on a two-camera machine vision system for the bayonets of automobile brake pads. *Measurement* 122 (2018), 106–116. <https://doi.org/10.1016/j.measurement.2018.03.017>
- [52] Yaxiong Xie, Jie Xiong, Mo Li, and Kyle Jamieson. 2019. MD-Track: Leveraging Multi-Dimensionality for Passive Indoor Wi-Fi Tracking. In *The 25th Annual International Conference on Mobile Computing and Networking* (Los Cabos, Mexico) (*MobiCom '19*). Association for Computing Machinery, New York, NY, USA, Article 8, 16 pages. <https://doi.org/10.1145/3300061.3300133>
- [53] L. Yujiri, M. Shoucri, and P. Moffa. 2003. Passive millimeter wave imaging. *IEEE Microwave Magazine* 4, 3 (2003), 39–50. <https://doi.org/10.1109/MMW.2003.1237476>
- [54] Youwei Zeng, Dan Wu, Jie Xiong, Jinyi Liu, Zhaopeng Liu, and Daqing Zhang. 2020. MultiSense: Enabling Multi-Person Respiration Sensing with Commodity WiFi. *Proc. ACM Interact. Mob. Wearable Ubiquitous Technol.* 4, 3, Article 102 (Sept. 2020), 29 pages. <https://doi.org/10.1145/3411816>
- [55] Youwei Zeng, Dan Wu, Jie Xiong, Enze Yi, Ruiyang Gao, and Daqing Zhang. 2019. FarSense: Pushing the Range Limit of WiFi-Based Respiration Sensing with CSI Ratio of Two Antennas. *Proc. ACM Interact. Mob. Wearable Ubiquitous Technol.* 3, 3, Article 121 (Sept. 2019), 26 pages. <https://doi.org/10.1145/3351279>
- [56] Youwei Zeng, Dan Wu, Jie Xiong, and Daqing Zhang. 2021. Boosting WiFi Sensing Performance via CSI Ratio. *IEEE Pervasive Computing* 20, 1 (Jan 2021), 62–70. <https://doi.org/10.1109/MPRV.2020.3041024>
- [57] Xu Zewei, Peng Jieru, and Chen Xianqiao. 2015. A method for vehicle three-dimensional size measurement based on laser ranging. In *2015 International Conference on Transportation Information and Safety (ICTIS)*. 34–37. <https://doi.org/10.1109/ICTIS.2015.7232075>
- [58] Daqing Zhang, Kai Niu, Jie Xiong, Fusang Zhang, and Shengjie Li. 2021. Location Independent Vital Sign Monitoring and Gesture Recognition Using Wi-Fi. *Contactless Human Activity Analysis* 200 (2021), 185.
- [59] Fusang Zhang, Kai Niu, Jie Xiong, Beihong Jin, Tao Gu, Yuhang Jiang, and Daqing Zhang. 2019. Towards a Diffraction-Based Sensing Approach on Human Activity Recognition. *Proc. ACM Interact. Mob. Wearable Ubiquitous Technol.* 3, 1, Article 33 (March 2019), 25 pages. <https://doi.org/10.1145/3314420>
- [60] Fusang Zhang, Daqing Zhang, Jie Xiong, Hao Wang, Kai Niu, Beihong Jin, and Yuxiang Wang. 2018. From Fresnel Diffraction Model to Fine-Grained Human Respiration Sensing with Commodity Wi-Fi Devices. *Proc. ACM Interact. Mob. Wearable Ubiquitous Technol.* 2, 1, Article 53 (March 2018), 23 pages. <https://doi.org/10.1145/3191785>
- [61] Jie Zhang, Yang Li, Haoyi Xiong, Dejing Dou, Chunyan Miao, and Daqing Zhang. 2022. HandGest: Hierarchical Sensing for Robust-in-the-Air Handwriting Recognition With Commodity WiFi Devices. *IEEE Internet of Things Journal* 9, 19 (2022), 19529–19544. <https://doi.org/10.1109/JIOT.2022.3170157>
- [62] Yue Zheng, Yi Zhang, Kun Qian, Guidong Zhang, Yunhao Liu, Chenshu Wu, and Zheng Yang. 2019. Zero-Effort Cross-Domain Gesture Recognition with Wi-Fi. In *Proceedings of the 17th Annual International Conference on Mobile Systems, Applications, and Services* (Seoul, Republic of Korea) (*MobiSys '19*). Association for Computing Machinery, New York, NY, USA, 313–325. <https://doi.org/10.1145/3307334.3326081>
- [63] Yin Zhou and Oncel Tuzel. 2018. VoxelNet: End-to-End Learning for Point Cloud Based 3D Object Detection. In *2018 IEEE/CVF Conference on Computer Vision and Pattern Recognition*. 4490–4499. <https://doi.org/10.1109/CVPR.2018.00472>